A NEW METHOD FOR ASSESSMENT OF DIRECTIONAL PERMEABILITY IN

CARBONATE FORMATIONS USING ELECTRICAL RESISTIVITY

MEASUREMENTS

A Thesis

by

EMMANUEL OLUWASEUN OYEWOLE

Submitted to the Office of Graduate and Professional Studies of
Texas A&M University
in partial fulfillment of the requirements for the degree of

MASTER OF SCIENCE

Chair of Committee,	Zoya Heidari
Committee Members,	Walter B. Ayers
	Michael C. Pope
Head of Department,	Daniel Hill

December 2015

Major Subject: Petroleum Engineering

ABSTRACT

The assessment of directional permeability in carbonate formations is challenging due to their complex pore structure and anisotropic pore-network properties. Previous studies have shown that permeability is controlled by the conducting pore network; which is the portion of the connected pore system that contributes to both fluid and electric current flow in the formation. Conventional permeability assessment techniques attempt to quantify the conductive pore network volume fraction using well-log-based estimates of acoustic or non-shale porosity. However, these porosity estimates do not represent the anisotropic conducting pore network as they fail to account for the directional pore-network connectivity in carbonate rocks. As a result, conventional well-log-based permeability assessment techniques are unreliable for quantifying directional permeability in carbonate formations. This thesis introduces a method for depth-by-depth assessment of the directional conducting pore network volume fraction and directional permeability using combined interpretation of well logs and pore-scale images from carbonate formations.

The proposed method takes advantage of the similarity between electric current and fluid flow paths in the rock-fluid system to estimate depth-by-depth directional conducting pore network volume fraction and permeability. In the field example presented, water saturation estimates were used to correct the electrical resistivity for the effect of hydrocarbon saturation. Then, well-log based rock classification was performed to identify

different petrophysical rock types in the formation. Three-dimensional pore-scale images were obtained from each rock type using an X-ray micro computed tomography scanner. Then pore-scale simulations of electrical current and fluid flow were conducted to develop conducting pore-network and permeability models for each rock type. Finally, these pore-scale models were applied for depth-by-depth assessment of directional conducting pore-network volume fraction and directional permeability.

The proposed method was applied in the pore-scale and well-log domain. In pore-scale domain, the method was used for the assessment of directional permeability in three carbonate rock types with complex pore structure. The pore-scale directional permeability estimates were cross-validated using permeability estimates obtained from a Lattice Boltzmann fluid flow simulator. In the well-log domain, the proposed technique was used to estimate permeability in the Canyon Reef formation of the SACROC oil field. The permeability estimates were cross-validated using available core measurements. The results showed a significant improvement using the proposed permeability assessment technique in both the pore-scale and well-log-scale domains. I observed a 52% and 34% decrease in the relative error associated with pore-scale and well-log domain permeability estimates, as compared to conventional porosity-permeability models.

DEDICATION

I dedicate this thesis to my loving parents, and to GOD, with whom all things are possible.

ACKNOWLEDGEMENTS

consortium on pore-scale modelling for providing some of the micro-CT images used in this work.

I would like to thank all my colleagues in the Multi-Scale Formation Evaluation Research Group, especially Mehrnoosh Saneifar, for their help in various aspects for this research. Finally, I would like to thank my parents for their love and support! I wouldn't have made it this far without you.

NOMENCLATURE

List of Acronyms

2D	Two-Dimensional
3D	Three-Dimensional
CT	Computed Tomography
GR	Gamma Ray
KNN	k-Nearest Neighbors algorithm
LBM	Lattice Boltzmann method
MICP	Mercury Injection Capillary pressure
PEF	Photoelectric Factor
PT	Pore Type
R35	Pore-throat radius corresponding to 35% of mercury saturation
SACROC	Scurry Area Canyon Reef Operators Committee

List of Symbols

A	Pore cross-sectional area, μm^2
a	Height of each pore-throat radius mode
b	Mean value of pore-throat radius in each mode
e	Permeability prediction error
BV	Number of black pixels in Micro-CT image

E	Average electric field magnitude
E_x	Average electric field magnitude in the direction of macroscopic flow
h	Height of micro-CT sample
F	Formation factor
J	Volume Current Density
k_{core}	Core permeability, md
k_{est}	Estimated permeability, md
L	Shortest Distance Between Inlet and Outlet of Electrical Current Flow Path
L_e	Effective Tortuous Path Traversed by Electrical Current
n	Number of core measurments
ϕ_c	Conducting porosity, fraction
σ	Electrical conductivity, S/m
ρ	Electrical Resistivity
p_{inlet}	Inlet Pressure for LBM simulator
P_{outlet}	Outlet Pressure for LBM simulator
τ	Tortuosity
TV	Total volume of pixels in segmented micro-CT image
R	Effective Electrical Resistance
v	Electric potential, volts

TABLE OF CONTENTS

LIST OF FIGURES

Page

1. INTRODUCTION AND LITERATURE REVIEW

Directional permeability assessment in carbonate formations is challenging due to the complex pore structure and anisotropic pore network properties of carbonate rocks. Permeability is controlled by the conducting pore network (Wempe and Mavko, 2002; Berg 2012); which is the portion of the connected pore space that supports fluid and electrical current flow in the rock-fluid system. The volume fraction of the conducting pore network; referred to as the conducting porosity, is not equivalent to the connected porosity (Katz and Thompson, 1987). The connected pore space is made up of poor-connected stagnant pores that do not actively contribute to fluid flow in the pore network. Consequently, the use of empirical correlations between permeability and total or connected porosity leads to prediction errors in permeability assessment.

Conventional permeability assessment techniques attempt to quantify the conducting porosity using well-log-based estimates of acoustic or non-shale porosity. These estimates of porosity do not represent the conducting porosity because they do not account for stagnant pore-spaces. They also do not account for the directional pore-network connectivity in carbonate rocks and are thus unreliable for directional permeability assessment. This thesis introduces as new method for quantifying the directional conducting pore network volume fraction and directional permeability in heterogeneous carbonate formations using conventional well logs and pore-scale images.

1.1 Background

Carbonate formations are highly susceptible to post-depositional diagenetic processes that significantly alter the primary porosity in carbonate rocks, resulting in isolated pores and pore systems with varying levels of connectivity (Lucia, 1995; Lucia, 2007; Sok et al., 2010). In addition to isolated pores, carbonate pore networks also consist poorly connected stagnant pores that constitute part of the connected pore volume, but do not actively contribute to the fluid or electrical flow in the formation (Fatt et. al., 1966). Permeability and electrical resistivity in carbonate formations are controlled by the conducting pore network (shown in **Figure 1.1**); which is the portion of the connected pore volume that contributes to both fluid and electric current flow in the formation (Katz and Thompson, 1987, Wempe and Mavko, 2002, Berg 2012). The continuous assessment of conducting pore-network from well-logs is however challenging.
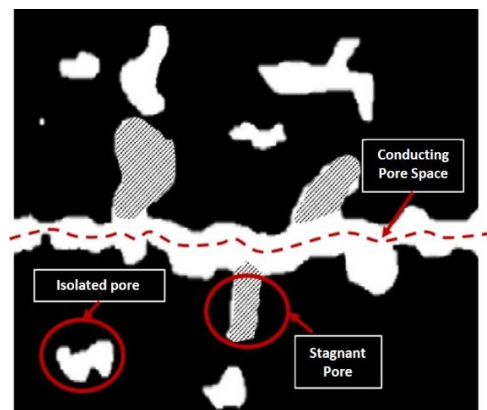
Figure 1.1—Carbonate pore-network model. Black and white regions represent the pore space and matrix, respectively. The shaded regions represents the stagnant pores. Modified from (Vik et al., 2007)

The assessment of conducting porosity and permeability in carbonate formations can be improved by taking advantage of the similarities between fluid and electrical current flow in the rock fluid system. Similar to fluid flow, electrical current is influenced by tortuosity, shape, and connectivity of the pore network (Archie, 1942; Wyllie and Spangler, 1952; Walsh and Brace, 1984). Several authors have tried to take advantage of this similarity by using core-based empirical resistivity-permeability correlations to estimate permeability from electrical resistivity measurements (Carothers, 1968; Ogbe and Bassiouni, 1978, Kosinski and Kelly, 1981, Mazac et. al., 1985). However, the use of these correlations often yields poor results due to the scatter in the permeability-resistivity crossplots (Huntley, 1987). The scatter can be attributed to the different rock types present in the formation and the strong influence of the pore-throat radius on permeability which is not accounted for in empirical resistivity-permeability correlations (Archie, 1942; Katz and Thompson, 1987)

Other authors have used percolation theory concepts to deduce the relationship between electrical resistivity and permeability (Ambegaokar et. al., 1971; Katz and Thompson, 1987). Using percolation theory arguments, Katz and Thompson (1987) derive a direct relationship between permeability and the formation factor given by

$$k = \frac{1}{226} l_c^2 \frac{\sigma}{\sigma_o},$$ (1)

where k is the permeability, σ_o is the electrical conductivity of the rock, σ is the electrical conductivity of the formation water and l_c is the smallest pore throat in the connect pore network determined from mercury injection capillary pressure (MICP) measurements. The equation has been successfully used to estimate permeability of various rock sandstone and carbonate rock types (Katz and Thompson, 1987; Garing et. al., 2014). However, the application of this method requires MICP measurements, which are not typically available at every desired depth in the formation. Furthermore, the method like resistivity-permeability correlations does not account the effect of hydrocarbon saturation on electrical resistivity measurements.

Other studies have deduced the pore-throat size and other pore-network properties that influence permeability from electrical resistivity measurements. By building on Archie's work on saturation assessment from electrical resistivity logs and permeability model developed by Kozeny-Carman (1927), Wyllie and Rose (1950) theoretically derived a relationship between electrical resistivity and permeability. The Wyllie and Rose permeability model is given by

$$k = a \frac{\phi^b}{S_{wi}^c}, \tag{2}$$

where k is the permeability in millidarcies, ϕ is the total porosity in percent, S_{wi} is the irreducible water in percent, and, *a, b, c* are all model parameters determined from empirical porosity-permeability correlations. Based on this general expression, various

4

other permeability relationships have been developed. These include Tixier's (1949), Timur's (1969) and Coates' (1974) equations which are given by

$$k = 62.5 \frac{\phi^6}{S_{wi}^2}, \tag{3}$$

$$k = 8.58 \frac{\phi^{4.4}}{S_{wi}^2}, \tag{4}$$

$$k = 4.90 \frac{\phi^4 (1 - S_{wi})^2}{S_{wi}^4}, \tag{5}$$

The irreducible water saturation (S_{wi}) in equations (2) to (5) characterizes the pore-throat size distribution of the rock. However, real time, in-situ, depth-depth assessment of irreducible water saturation requires NMR measurements. In the absence of NMR logs it is common practice to assume a constant value for irreducible water saturation in the formation. This assumption transforms equations (2) to (4) back into simple porosity-permeability correlations. Although these correlations have been successfully applied in siliciclastic formations, their use leads to large prediction errors in carbonate formations. This error stems from the multi-scale heterogeneity and complex pore structure of carbonate rocks (Lucia, 1995)

Previous studies have shown that permeability is controlled by the conducting pore network; which is the portion of the pore volume that supports fluid and electrical current flow (Katz and Thompson, 1986; Wempe and Mavko, 2002; Berg 2012). The conducting

pore network does not include isolated vuggy pores or poorly connected stagnant pores-space which constitute part of the connected pore volume but do not actively contribute to fluid flow in the formation.

For well-connected siliciclastic rocks having predominantly intergranular pores with uniform pore size distributions, the conducting, connected and total porosity are close (Wempe and Mavko, 20012). Consequently, porosity-permeability correlations can be used for permeability assessment in sandstone formations. On the other hand, carbonates include a variety of pore types with varying level of connectivity (Dunham, 1962; Choquette and Pray, 1970; Lucia, 1995). Some of these pores are isolated and poorly connected due to the complex heterogeneous pore systems created by diagenetic processes such as dissolution and dolomitization. As a result, carbonate formations exhibit poor correlations between permeability and total porosity. Consequently, the use of empirical total porosity-permeability correlations is not reliable for permeability assessment in carbonate formations. Furthermore, permeability-porosity correlations are based on scalar quantities like porosity and irreducible water saturation and provide little information about the anisotropic nature of permeability. The directional permeability is a function of the directional pore network connectivity which is reflected in the directional conducting pore network of the formation.

Well-log-based assessment of the directional conducting pore-network volume fraction (i.e., conducting porosity) is challenging. Previous studies have used acoustic well-logs to quantify the conducting pore-network in carbonate formations (Brie et. al., 1985; Kazatchenko et. al., 2003). These studies took advantage of the effect of isolated vuggy porosity and fractures on acoustic wave propagation. Acoustic waves travel faster in dual porosity carbonate rocks with isolated and connected pores than in carbonate rocks with intergranular porosity. Consequently, the porosity estimated from the Wyllie-time average equation (Wyllie et. al., 1956) is lower than the actual total porosity measured from a helium porosimeter. The authors refer to the Wyllie-time average porosity as the effective porosity and assert that it is representative of the conducting pore volume (Kazatchenko et. al., 2003). However, since acoustic porosity estimates do not account for dead-end pore spaces they are not equivalent to the conducting pore volume.

Well-log-based assessment of conducting pore network volume fraction and permeability can be improved by taking advantage of the similarity between fluid flow and electrical current flow in porous media. Like fluid flow, electrical current is influenced by the pore size distribution, and tortuosity of the pore network (Archie, 1942; Winsauer et. al., 1952, Wyllie and Spangler, 1952). By modelling the pore network as a bundle of tortuous capillary tubes Wyllie and Rose, (1950) developed a theoretical model for the formation factor introduced by Archie (1942). Wyllie and Rose formation factor expression is given by

$$F = \frac{\tau}{\phi},$$ (6)

where, F is the formation factor, ϕ is the porosity and τ is the tortuosity is defined by Rose and Bruce (1949) as

$$\tau = \left(\frac{L_e}{L}\right)^2,$$ (7)

where L_e is the effective tortuous path traversed by the current and L is the shortest distance connecting the two ends of the traversed path shown in **Figure 1.2**.
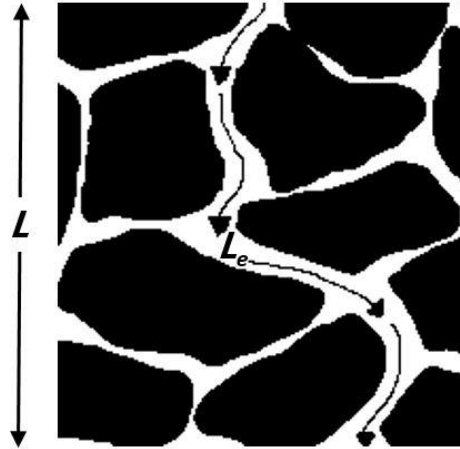
Figure 1.2—Tortuous electrical current flow path. L_e is the effective tortuous path traversed by the current and L the shortest distance connecting the two ends of the traversed path.

The formation factor relationship presented in Equation (8) was subsequently re-derived by Wyllie and Spangler, 1952, and Walsh and Brace (1984). However, these authors did not account for the effect of the variable cross sectional area of electrical current carrying capillary tubes on the electrical resistivity. Taking into account the variable cross-sectional area created by the constriction of the pore-space at the pore-throat produces expression for the formation factor given by

$$F = C \frac{\tau}{\phi_c},$$ (8)

where F is the formation factor, τ is the tortuosity of the flow path, ϕ_c is the conducting pore-network, and C is the constriction factor (Berg, 2012). The constriction factor is a geometric factor describing the reduction in the effective flow area from the pore body to the pore throat.

Based on Equation (9) the conducting pore-network can be determined from electrical resistivity, tortuosity and constriction of the pore space. However, there is no method for independently quantifying the tortuosity and constriction factor from well logs. Furthermore depth-depth assessment of the formation factor from well logs is very challenging due to the effect of fluid saturations on electrical resistivity well logs. This limitation can be addressed by using numerical simulation of electrical current flow in three dimensional pore-scale images to develop models for the conducting pore-network in the formation. Several studies have used three dimensional X-ray microtomography

(micro-CT) images to numerically derive electrical resistivity, directional permeability and tortuosity in porous media (Chen and Doolen, 1998; Dong, 2007; Chi and Heidari, 2014; Sok et. al., 2010; Øren and Bakke, 2002). However, due to the multi-scale heterogeneity of carbonate formations, reliable rock classification must be performed to identify the different rock types in the formation. After rock classification is conducted, pore-scale conducting porosity and permeability models developed for each rock type can then be applied for depth-by-depth assessment of directional permeability in the formation. This thesis introduces a method for estimating directional permeability and directional conducting porosity in carbonate formations based on electrical resistivity well-logs and pore-scale numerical simulations of electrical current flow in carbonate rocks.

1.2 Problem Statement

The assessment of directional permeability in carbonate formations is challenging due to the complex pore structure and anisotropic pore-network properties of carbonate rocks. The permeability is controlled by the conducting pore network; which is the portion of the connected pore volume that contributes to both fluid flow in the formation. This same portion contributes to electrical current flow in the rock-fluid system. Well-log based assessment of the conducting pore-network remains a challenge for petroleum engineers and geoscientists. Existing permeability assessment techniques attempt to quantify the effective porosity using well-log-based estimates of acoustic or non-shale porosity.

However, these estimates of porosity do not represent the anisotropic conducting pore volume as they fail to account for the directional pore-network connectivity in carbonate rocks. As a result, conventional well-log-based permeability assessment techniques are not reliable for quantifying directional permeability in carbonate formations. This thesis introduces a new method for the depth-by-depth assessment of directional conducting pore-network and directional permeability using combined interpretation of well logs and pore-scale images from carbonate formations.

1.3 Research Objectives

The main objective of this thesis is to develop and apply a new directional permeability assessment technique based on electrical conducting pore-network estimates derived from pore-scale images and electrical resistivity well-logs. The detailed list of objectives for this research are as follows:

I. Introduce a workflow of estimating directional conducting pore-network volume fraction (i.e., conducting porosity) and directional permeability in carbonate formations based on electrical resistivity well-logs and pore-scale numerical simulations of electrical current flow in three dimensional micro-CT images.

II. Estimate directional conducting pore network volume fraction in the pore-scale and well-log domain by using numerical simulations of electrical current flow to characterize directional pore-network properties.

III. Apply the proposed permeability assessment technique to estimate pore-scale

directional permeability in different carbonate rock types.

IV.   Develop and apply pore-scale conducting porosity and permeability models for depth-by-depth assessment of conducting porosity and permeability in the Canyon Reef formation of the SACROC oil field.

1.4 Method Overview

Figure 1.3 shows the workflow describing the proposed permeability assessment technique. First, joint interpretation of well-logs is conducted to assess the petrophysical and compositional properties of the formation. Then, petrophysical rock classification is performed based on the depth-by-depth estimates of petrophysical properties, mineralogy and MICP measurements. High-resolution three-dimensional pore-scale image of each rock type are obtained using an X-ray tomography machine. Pore-scale numerical simulations are used to estimate the directional conducting pore network volume fraction and permeability of the micro-CT images in each rock class. The results of the pore-scale simulations were used to develop conducting porosity and permeability models for each rock class. Deep resistivity well-logs are corrected for fluid saturation using Archie's equation. Then the conducting porosity models, deep resistivity logs and fluid corrected resistivity well-logs are all used for the depth-by-depth assessment of conducting porosity in the formation. Finally, the pore-scale permeability models and well-log based estimates of conducting porosity are used for the depth-depth assessment of directional permeability in the formation.
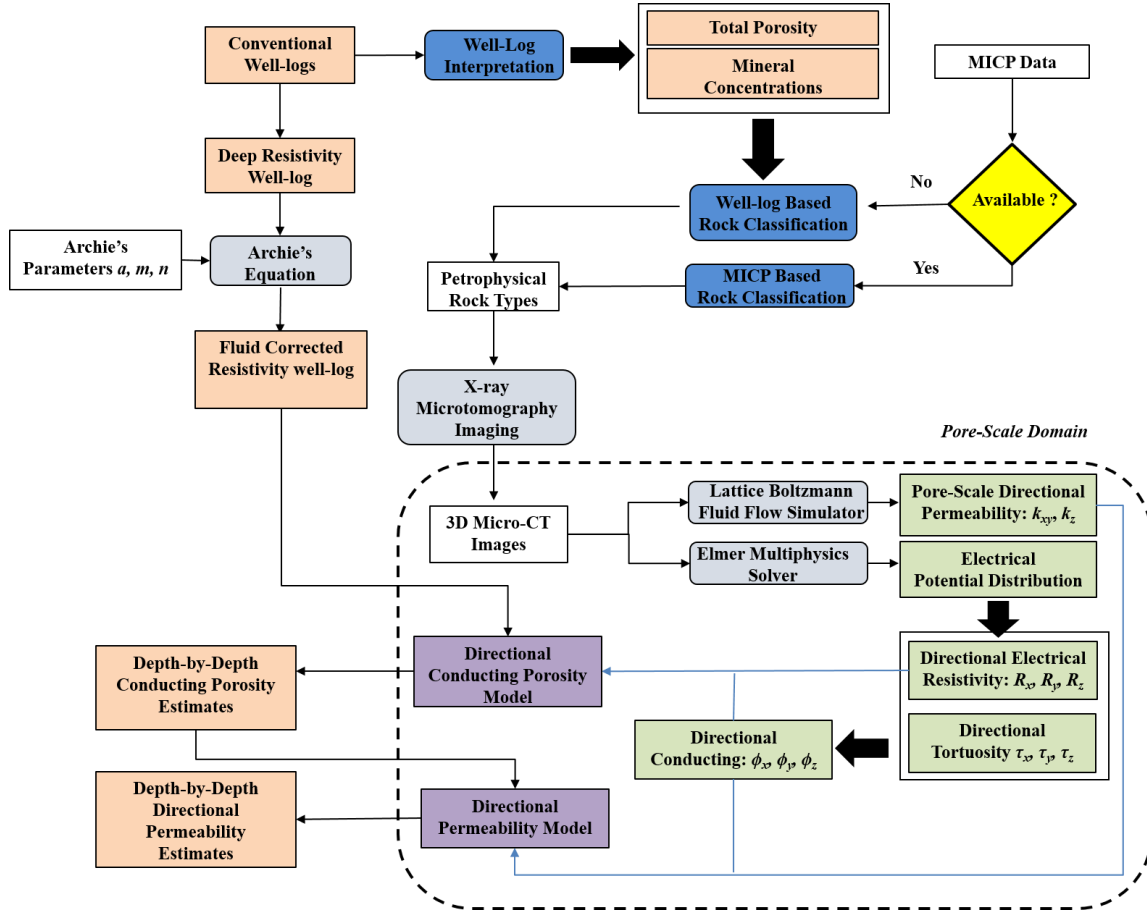
Figure 1.3—Workflow for the proposed permeability assessment technique.

1.5 Outline of Thesis

This thesis consists of five sections. Section 2 provides a description of each process in the integrated workflow used to assess conducting porosity and permeability. The section provides detail description of the well-log interpretation, petrophysical rock classification,

the pore-scale imaging process and various numerical methods used to simulate current and fluid flow in the rock-fluid system.

Section 3 elaborates on the pore-scale application of the proposed method to estimate directional conducting pore network volume fraction and permeability of three carbonate rock samples. The results of the pore-scale numerical simulations of fluid and electrical current flow are presented to demonstrate the similarities between fluid and electrical current flow paths. Estimates of the connected and conducting porosity are presented to demonstrate the difference between the connected and conducting porosity. Finally the directional permeability estimates based on the proposed technique are compared to empirical porosity-permeability correlations.

Section 4 presents the application of the proposed method to estimate permeability and conducting porosity in the SACROC oil field. The details of the methods used for well-log interpretation, petrophysical rock classification are presented. The pore-scale models used for the assessment of conducting pore-network and permeability are also presented. The final well-log domain permeability estimates from the proposed method are compared to permeability estimates from conventional porosity-permeability correlations.

Finally, Section 5 summarizes the main results and conclusion of this thesis and provides recommendations for future work.

2. METHOD

This section describes the methods used to estimate numerical simulation methods used for the pore-scale assessment of the directional permeability and conducting porosity in this thesis. The first step of the process is acquiring 3D pore-scale images of representative rock samples using X-ray tomography (micro-CT) imaging. Image processing techniques are applied to convert the gray-scale micro-CT images into segmented binary images which are used as inputs for the numerical simulation of fluid and electrical current flow in the 3D pore-scale images. The electrical resistivity of the pore network is obtained by solving the Laplace equation for the electrical potential distribution within 3D micro-CT images. The Lattice Boltzmann method is used to simulate fluid flow in each micro-CT image and Darcy's law is used to estimate the permeability in the direction of fluid flow.

2.1 3D Pore-Scale Imaging

3D pore-scale images used in this thesis were acquired using an X-ray micro-computed tomography (micro-CT) scanner. Micro-CT imaging is a non-destructive 3D imaging technique used to characterize the internal structure of a material at a micron-level spatial resolution. Micro-CT scanners use x-rays to penetrate the sample from different angles to create a series of two-dimensional (2D) x-ray absorption images of a rotating sample specimen. The 2D absorption images are reconstructed into a digital three dimensional micro-CT image by a computer algorithm based on the mathematical principles of tomography. The final output is a stack of two dimensional gray-scale images of the 3D

volume. **Figure 2.1** shows an example of a 2D gray-scale image slice of a carbonate rock sample. The level of x-ray absorption correlates to the material density therefore the intensity of each pixel represents the density of the material at a given point. Consequently, the low-density pores are represented by the dark pixels, whereas the high density calcite grains are represented by the light gray pixels.
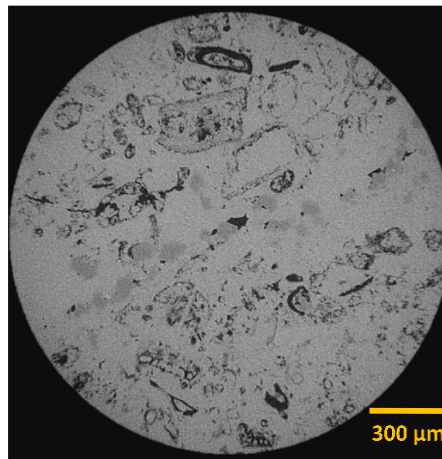
Figure 2.1—A 2D gray-scale image slice of a carbonate rock sample. The pore space is represented by the black pixels while the mineral grains are represented by the light gray pixels

2.1.1 Instrumentation

Majority of the micro-CT images in this thesis were obtained using a Zeiss Xradia 520 versa desk-top X-ray micro-tomography scanner at the W.D. Von Gonten Laboratories (**Figure 2.2**). The sample, noted by (1) in Figure 2.1 was placed on the sample positioning

stage, noted by (2). A series of electronic motion controllers were used to position the specimen in the center of the x-ray beam line, noted by (3). High energy x-ray beams generated from the x-ray source, noted by (4), pass through an aperture, noted by (5). X-ray source filters (6) were used to narrow the x-ray energy spectrum range. The resulting absorption profile is captured by a high resolution x-ray detector system (item 7). The three dimensional images were reconstructed on a desktop computer (not shown) using a built-in X-radia software package.
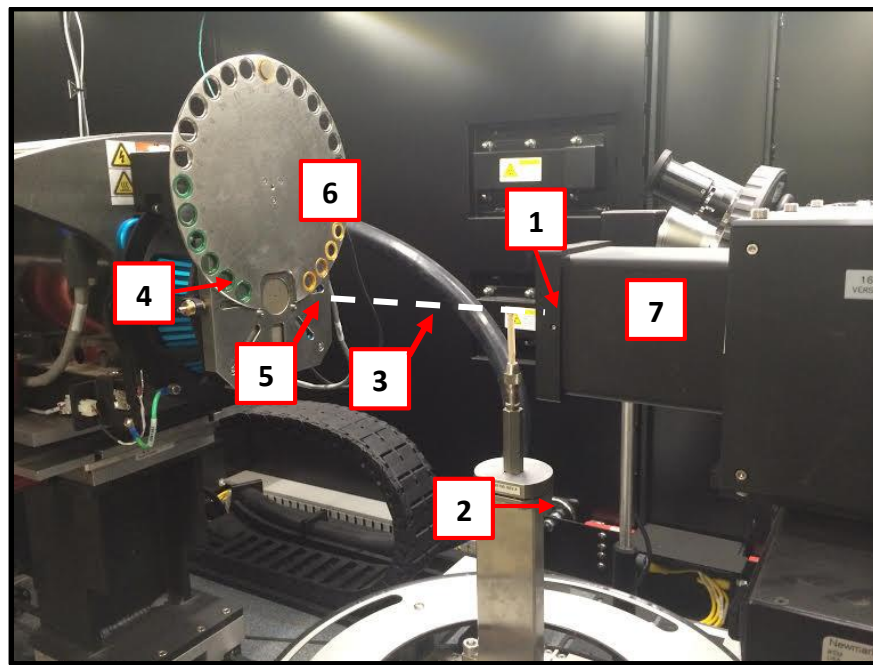
Figure 2.2—Zeiss Xradia 520 versa desk-top X-ray micro-tomography scanner at the W.D. Von Gonten Laboratories. (1) rock sample, (2) sample positioning stage, (3) x-ray beam line, (4) x-ray source, (5) x- ray aperture, (6) x-ray source filter, (7) x-ray detection system

2.1.2 Sample Preparation

The micro-CT samples used in this thesis were obtained from 4 inch diameter whole core samples vertical to the bedding plane. The core samples were cut into smaller half inch samples for micro-CT imaging. **Figure 2.3** shows an example of the samples used for micro-CT imaging is shown in**.**
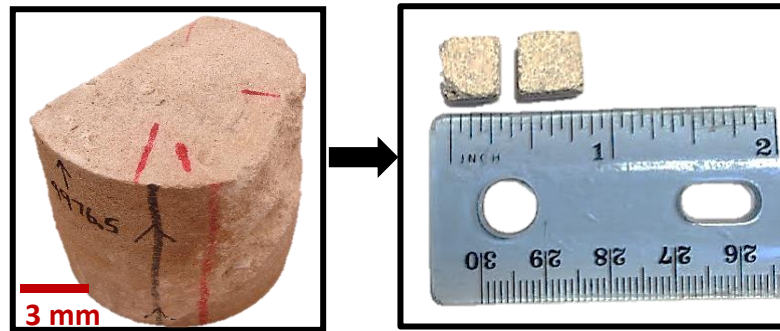
Figure 2.3—Example of core samples used for micro-CT imaging (a) 4 inch core sample, (b) quarter inch samples used for micro-CT imaging.

2.1.3 Image Segmentation

An image segmentation process is required to distinguish the pore space from the matrix grains and convert the gray-scale image into a binary image. Fiji ImageJ (Schindelin et al., 2012), an open source scientific imaging processing software was used to convert the gray-scale images into a sequence of binary images, where black and white regions represent pixels represent the pores and white pixels represent the grains. The *threshold*

function available in ImageJ was used to segment the gray-scale images. The algorithm segments partitions the each image pixel based on its intensity.

Figure 2.4 shows an example of a voxel intensity histogram. The first peak in the gray-intensity histogram corresponds to the high-intensity pixels representing the grains while the second peak corresponds to the low-intensity pixels representing the pores. A gray-scale threshold value is selected at the transition between the grains and pores. Pixels with intensity values higher than the threshold values are partitioned from pixels with intensity values lower that the threshold value. If the thresholding segmentation does not satisfy a visual inspection, adjustments are made using different image processing techniques to ensure the segmented image is representative of the original gray-scale image.
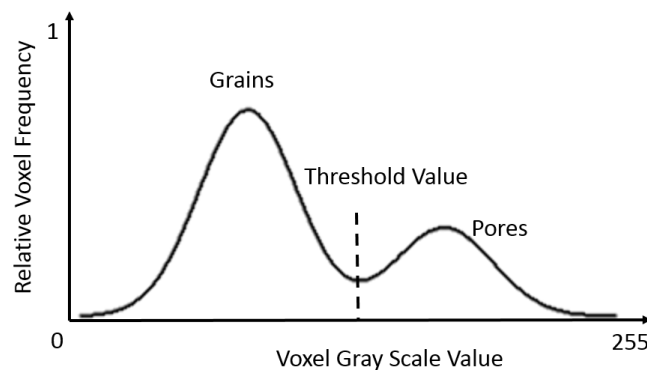
Figure 2.4—Example of a voxel gray-scale histogram. The first peak in the gray-scale histogram corresponds to the high-intensity pixels representing the grains while the second peak corresponds to the low-intensity pixels representing the pores.

Figure 2.5 shows an example of a segmented gray-scale image. The pore spaces are represented by black pixels while the grains are represented by white pixels.

<div align="center">(a)   (b)</div>
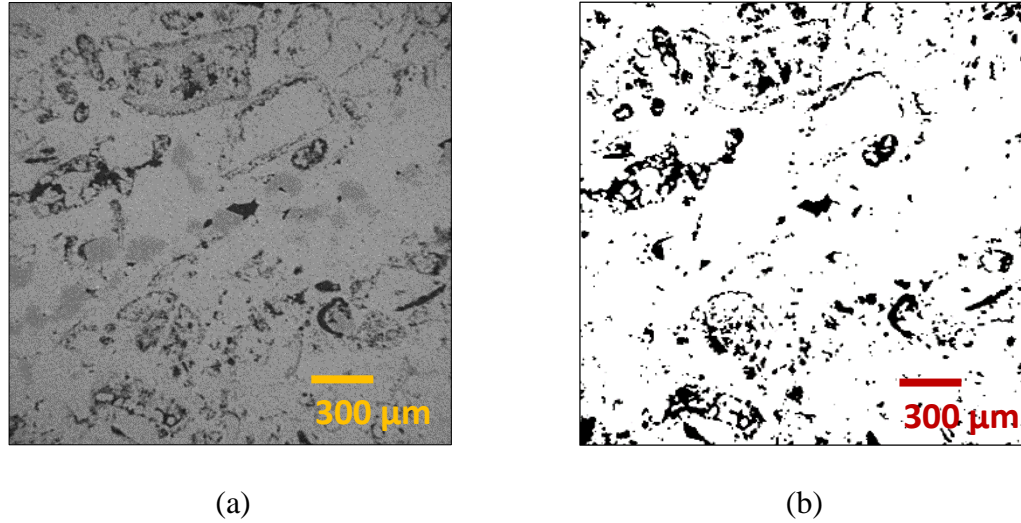
Figure 2.5—(a) Gray-scale micro-CT image. (b) Segmented binary image. The pore spaces are represented by black pixels whereas the grains are represented by white pixels.

2.1.4 3D Image Post-Processing and Renditions

The 2D segmented slices were reconstructed using the ImageJ *BoneJ volume viewer* plugin (Douebe et. al, 2010) available on Fiji ImageJ to visualize the 3D segmented image the stack. This plugin shows stacks as volumes in a 3D- Cartesian (xyz)-space. In addition to the volume rendering, the *BoneJ 3D viewer plugin* was used to extract and visualize the 3D pore space from the segmented stack. **Figure 2.6** shows an example of the reconstructed image stack and the 3D pore-space rendition obtain from ImageJ.
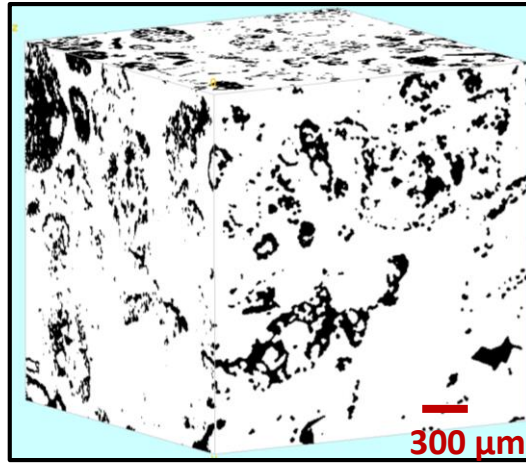
(a)
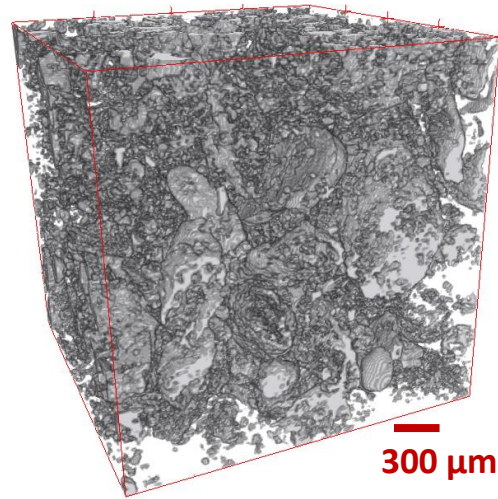
(b)

Figure 2.6—(a) 3D ImageJ rendition of segmented image (b) 3D Rendition of pore network extracted from segmented image.

2.2 Pore Scale Numerical Simulations

This section outlines the various pore-scale numerical simulations used to calculate the conducting porosity and permeability of the 3D micro-CT images.

2.2.1 Electrical Current Flow Simulation

The electrical resistivity of each pore-scale image is obtained by solving the Laplace equation for the electrical potential distribution within the pore-network.

The Laplace equation is given by

$$\nabla \cdot (\sigma \cdot \nabla v) = 0, \tag{9}$$

where, σ is the electrical conductivity and v is the electric potential at each point in the pore network. I assumed the pore-space in the micro-CT image was fully saturated with formation water and the conductivity, σ in Equation (9) is equivalent to the conductivity of formation water. The electric current in the pore network was calculated from the electric field potential using Ohm's law which is given by

$$\vec{J} = -\sigma \nabla v, \tag{10}$$

where $\vec{J}$ is the volume current density. The effective resistance of the pore network was then obtained by calculating the total power in the conducting pore network system which is given by

$$P = \int_{\Omega} \nabla \phi \cdot \sigma \nabla \phi d\Omega, \tag{11}$$

The effective directional electric resistance is given by,

$$R = \frac{V^2}{P}, \tag{12}$$

where R is the effective resistance and V is the electrical potential difference across the entire micro-CT sample. The sample resistivity can be estimated from the effective resistance. The sample resistivity is given by

$$\rho = \frac{A}{h}R,$$ (13)

where ρ is the resistivity, A is the area of each 2D micro-CT slice in pixels and the h is the height of the sample in pixels.

2.2.1.1 Electrical Current Simulation Workflow

Figure 2.7 shows the electrical current simulation workflow used in this thesis. First, Delaunay triangulation was used to generate a tetrahedral mesh of the voxelized 3D pore-space extracted from the micro-CT images. Then, *Elmer*, a finite element solver was used to solve for the total current flow within the 3D pore-network. Finally the electrical resistivity in any desired direction was calculated from the total current and electric potential difference across the pore-network.
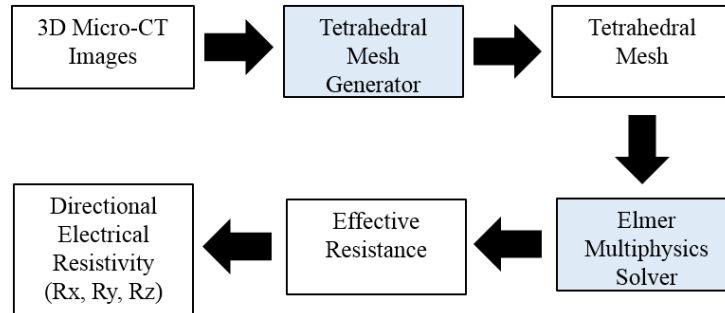
Figure 2.7— Pore-scale electrical resistivity computation workflow

2.2.1.2 Pore-Space Mesh Generation

Delaunay triangulation was used to generate a tetrahedral mesh of the 3D pore space based on the procedures and algorithms developed by (Fang and Boas, 2009). **Figure 2.8** shows an example of a tetrahedral mesh of a 3D pore-network.

(a)   (b)
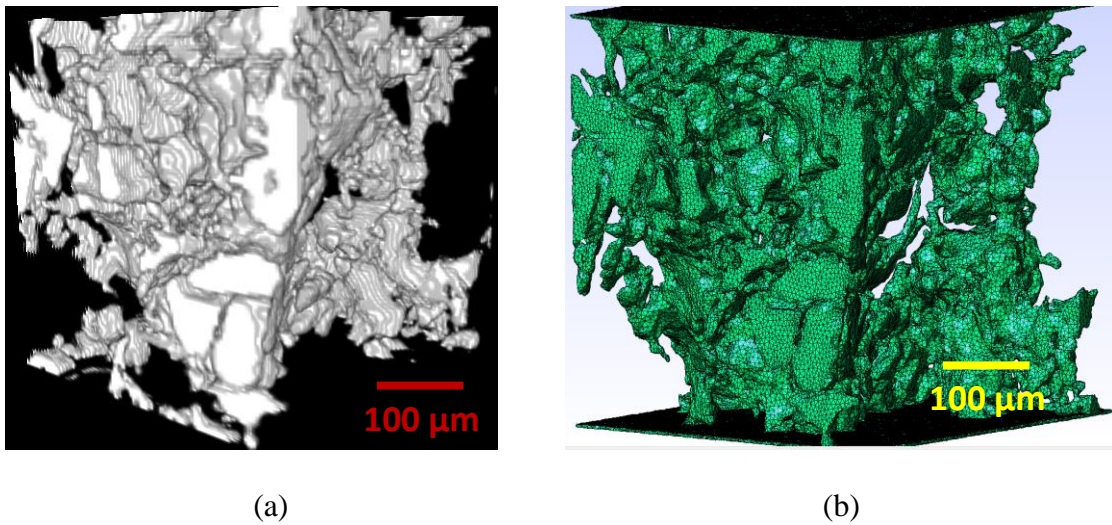
Figure 2.8—(a) Voxelized 3D pore network, (b) tetrahedral mesh of a 3D pore-network.

2.2.1.3 Electrical Current Simulation

After mesh generation the electrical potential distribution and the effective electrical resistance of the pore-network was obtained using *Elmer,* an open source multiphysics solver created by the center for IT science in conjunction with various Finnish Universities. The inputs to the solver include the tetrahedral mesh generation and the

electrical potential difference. The solver outputs determines the, total current, effective

resistance and electrical potential at each point within the pore network.

2.2.2 Electrical Tortuosity Calculation

The electrical pore-network tortuosity was estimated from the electric field streamline

tortuosity introduced by (Matyka and Koza, 2012). The streamline tortuosity is given by

$$\tau_x = \frac{\sum |E|}{\sum |E_x|}, \tag{14}$$

where, $|E|$ is the average electric field magnitude at each point in the pore network and

$|E_x|$ is the average electric field magnitude in the direction of macroscopic flow at each

point in the pore network **(Figure 2.9)**.
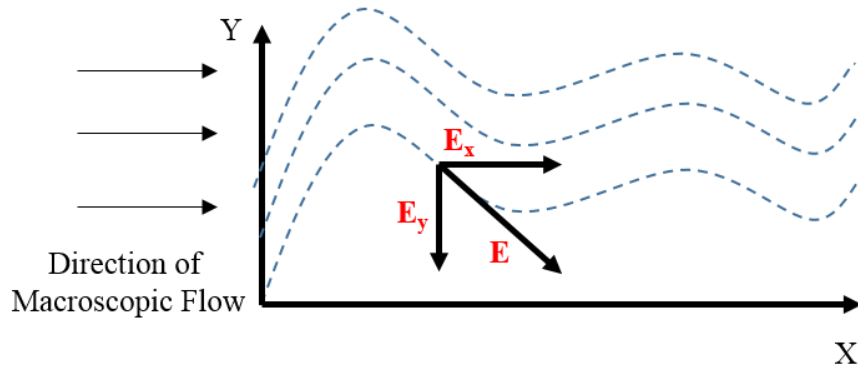
Figure 2.9—Illustration of tortuosity computation from electrical current streamlines.

2.2.3 Directional Conducting Pore-network Assessment

The conducting pore-network in the formation can be obtained from the expression for the formation factor introduced by Wyllie and Rose (1950), and Berg (2012). The Wyllie and Rose expression for the formation factor is given by

$$F = \frac{\tau}{\phi}, \tag{15}$$

where, ϕ is the total porosity and τ is the tortuosity. However, the electrical resistivity is a function of the conducting porosity, not the total porosity. Therefore the conducting porosity can be expressed as

$$\phi_c = \frac{\tau}{F}, \tag{16}$$

where, ϕ_c is the conducting pore-network. The electrical tortuosity and formation factor are both directional pore-network properties that vary in the vertical and horizontal direction directions. Consequently, the conducting pore-network defined in Equation (16) is a directional pore network property that has a magnitude equivalent to the conducting porosity and direction determined by the electrical current flow in the rock-fluid system.

2.2.4 Fluid Flow Simulation

To obtain develop pore-scale relationship between permeability and the conducting pore-network, I estimated directional permeability from fluid flow in each 3D pore-scale image. I used the Lattice Boltzmann method to simulate fluid flow in three-dimensional pore-

network. The Lattice Boltzmann method is a discrete computational fluid dynamic method based upon the Boltzmann equation. The lattice Boltzmann method is applied as an alternative to solving the Naviers stokes equation for complex fluid flow problems. The method has been widely applied to simulating fluid flow in porous media (Chen and Doolen, 1998; Dong, 2007; Chi and Heidari, 2014; Sok et. al., 2010; Øren and Bakke, 2002)

The pore-scale directional permeability in this thesis was estimated using Palabos (2013), an open source parallel lattice Boltzmann solver to simulate single-phase fluid flow in all three directions of the 3D micro-CT image. The inputs to the simulator include a voxelized segmented micro-CT image, a predetermined pressure gradient, the dimensions of the voxelized image and the fluid viscosity. The solver output the average velocity within the pore network

From the average velocity the permeability was calculated using Darcy's law,

$$U = -\frac{k}{\mu} \frac{p_{inlet} - p_{outlet}}{h}, \tag{17}$$

Where U is the fluid velocity, μ is the fluid viscosity, P_{inlet} is the inlet pressure, P_{outlet} is the outlet pressure and h is height of the voxelized segmented image.

3. PORE-SCALE DIRECTIONAL PERMEABILITY ASSESSMENT

This section presents the application of the proposed method to carbonate rocks with different rock fabric and complex pore structure. The proposed method was use to estimate directional conducting pore-network and permeability of 3D micro-CT images obtained from the Pore Scale Modelling Consortium at the Imperial College, London. The permeability estimates obtained using the proposed technique were compared to permeability estimates from empirical porosity permeability correlations.

3.1 Introduction

Assessment of directional permeability has been a challenge in anisotropic carbonate formations with complex pore structure. Unlike siliciclastic rocks which are dominantly have intergranular pores with uniform pore size distributions, carbonate pore systems feature a wide array of pore types with varying level of connectivity (Dunham, 1962; Choquette and Pray, 1970; Lucia, 1995). Some of these pores are isolated and poorly connected due to the complex heterogeneous pore systems created by diagenetic processes. As a result, carbonate formations have poor correlations between permeability and porosity. Thus, permeability-porosity correlations are commonly not suitable for to directly determine permeability in carbonate formations.

Previous studies tried to incorporate critical pore-network properties into carbonate permeability assessment by classifying carbonate rocks into different rock types and applying specific porosity-permeability correlations in each rock class. Methods such as the rock fabric number (Lucia, 1999) and Lonoy's (Lonoy, 2006) pore type classification, classify various rocks based on the rock texture observe in thin section images and the dominant pore size in each rock class. Other methods such as the Leverett's J-function (Leverett, 1941) and Winland's R35 (Pittman, 1992) characterize rocks based on pore-throat size distributions obtained from saturation-dependent mercury capillary pressure measurements. These rock classification permeability assessment techniques attempt to describe and quantify the amount of connected pore space available for fluid flow. However, fluid flow is controlled by the conducting (not the connected) porosity; which is the portion of the pore space that actively contributes to fluid and electrical current flow in the rock-fluid system. Furthermore, these permeability assessment techniques do not account for the anisotropic pore-network properties that affect directional permeability.

The assessment of permeability and conducting pore-network in carbonate rocks can be improved by taking advantage of the similarity between fluid flow and electrical current flow in porous media (Katz and Thompson, 1987). Similar to fluid flow, electrical current is influenced by the size, shape, and connectivity of the pore-space (Archie, 1942). Previous studies have also used percolation theory arguments and laboratory measurement to demonstrate that fluid and electrical current flow are both controlled by a portion of the connected pore volume (Katz and Thompson, 1987). This portion of the pore volume

29

corresponds to the conducting pore-network. Therefore, the conducting pore-network can be obtained by quantifying the portion of the pore volume that contributes to electrical current flow.

However deducing the conducting porosity directly from electrical resistivity well log measurements in carbonate formations can be very challenging due to complex pore morphology of carbonate rocks. This limitation can be addressed by numerically deriving the electrical resistivity from three dimensional pore-scale images of rock samples in the formation. In the past decade, recent studies have used high-resolution X-ray micro-CT images to numerically derive the permeability and electrical resistivity in both sandstone and carbonate rocks (Øren and Bakke, 2002; Chen and Doolen, 1998). Therefore the conducting porosity-permeability relationship can be obtained by simulating electrical current and fluid flow in 3D micro-CT images of representative rock samples in the formation. The pore-scale conducting-permeability models can then be applied for depth-by-depth assessment of directional permeability in the formation.

This research introduces new method for the assessment of directional conducting pore-network volume fraction based on numerical simulations of fluid and electrical current flow in pore-scale core images from typical rock types in the formation. I successfully applied the introduced method to estimate pore-scale directional conducting pore-network and permeability in three carbonate rock types with complex pore structures. I compared

the permeability estimates obtained from the proposed method to permeability results obtained from the application of conventional correlations between connected porosity and permeability.

3.2 3D Pore-Scale Images of Carbonate Rock Samples

Figure 3.1 shows the 3D pore-scale images of the three carbonate rock types used in this study. The images were obtained from the pore-scale modelling group at the Imperial College, London.

300 µm	300 µm	300 µm
Sample 1	Sample 2	Sample 3
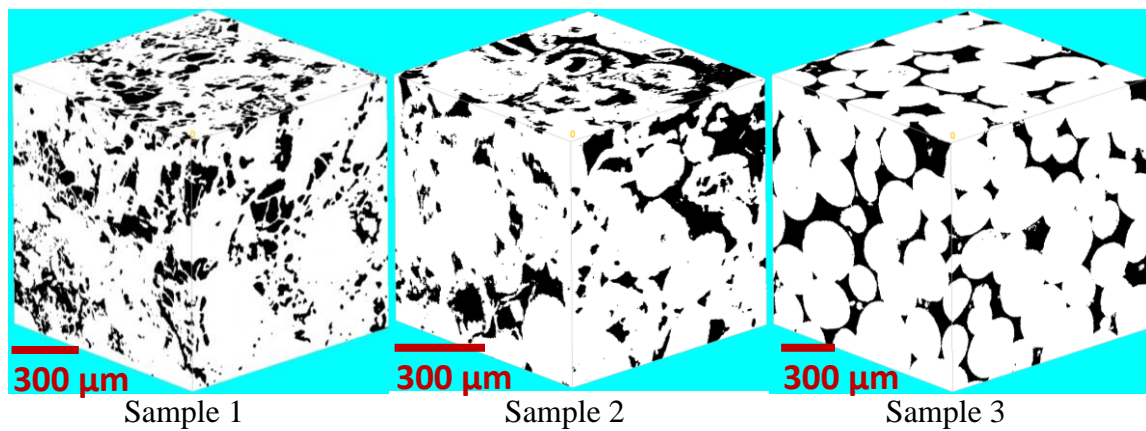
Figure 3.1—3D micro-CT pore-scale images of the three carbonate rock samples used in the study

3.3 Directional Pore-Network Volume Fraction Assessment

First, each pore-scale image was subdivided into smaller 8 to 10 smaller subsamples to model the relationship between conducting pore-network and permeability in each rock type. Then a finite element solver is used to solve the Laplace's equation for the electrical potential distribution within the 3D pore network. Finally ohm's law is used to calculate the electrical current and resistivity in all desired directions (x, y, z) from the electrical potential distribution.

The input for the electrical current simulator is a tetrahedral mesh of the binarized 3D micro-CT image shown in **Figure 3.2**.
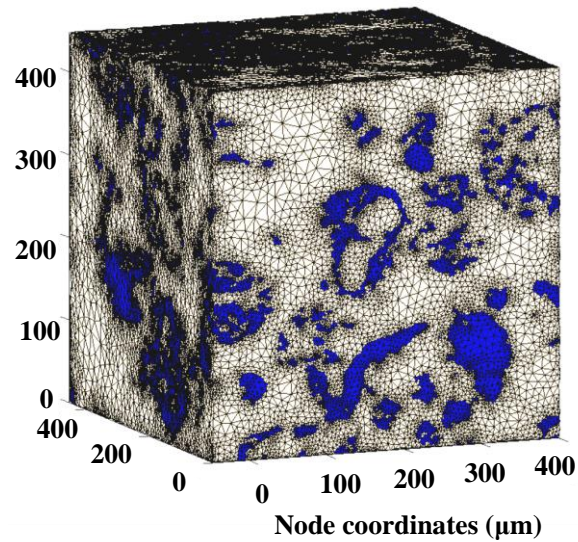
Figure 3.2—Delaunay Triangulation of 3D tetrahedral mesh. The beige and blue regions represent the grains and pores, respectively

The mesh is obtained through Delaunay triangulation of the voxelized 3D micro-CT image using a procedure created and developed by (Fang and Boas, 2009). I assumed that the grains are non-conductive and the pore space is fully saturated with conductive saline water of resistivity similar to the formation water. The electrical potential at the top and bottom of the pore network were set to boundary conditions of 10 and 0 volts respectively. A zero flux boundary was imposed on the non-conductive grains.

After obtaining the electric potential distribution with the pore-network, I estimated the tortuosity in all desired direction from the electrical flow streamlines. The streamline tortuosity is obtained by calculating the ratio between the average length of the electrical potential streamlines within the pore-network and height of the micro-CT sample.

To calculate the directional permeability in all desired direction in each micro-CT image I used the lattice Boltzmann method (LBM) to simulate fluid flow in the voxelized micro-CT image. In lieu of solving the macroscopic Navier stokes equation, the lattice Boltzmann method simulates the flow of a Newtonian fluid by discretizing the Boltzmann transport equation on a lattice mesh. I use Palabos (2013), an open source parallel lattice Boltzmann solver to simulate single-phase fluid flow in all three directions of the 3D micro-CT image. Finally, directional permeability is calculated from Darcy's law.

3.4 Connected Porosity Assessment

To compare the proposed method with empirical porosity permeability correlations I estimated the connected porosity for the micro-CT image subsamples in each rock type. I used Fiji ImageJ, an open source scientific imaging processing software to estimate the connected porosity in each pore-scale image. The procedure for calculating the connected porosity is outlined in this section.

First, the *BoneJ purify* command was used to eliminate the isolated pore space from the segmented image, then the *volume fraction* command was used to calculate the connected porosity. The total porosity is defined by

$$\phi_t = \frac{BV}{TV}, \tag{23}$$

where, ϕ_t is the total porosity, BV is the number of black pixels in the segmented image stack and TV is the total number of pixels in the segmented image stack. Similarly the connected porosity is defined as

$$\phi_c = \frac{BV_{purify}}{TV}, \tag{24}$$

where, ϕ_t is the total porosity, BV_{purify} is the number of black pixels in the segmented image stack after the *purify* command has been implemented and TV is the total number of pixels in the segmented image stack. **Figure 3.3** is a side-by-side comparison between

a slice of segmented image before and after the purify command was implemented. **Figure 3.4** is similar comparison between the three dimensional pore-network before and after the purify command was implemented.
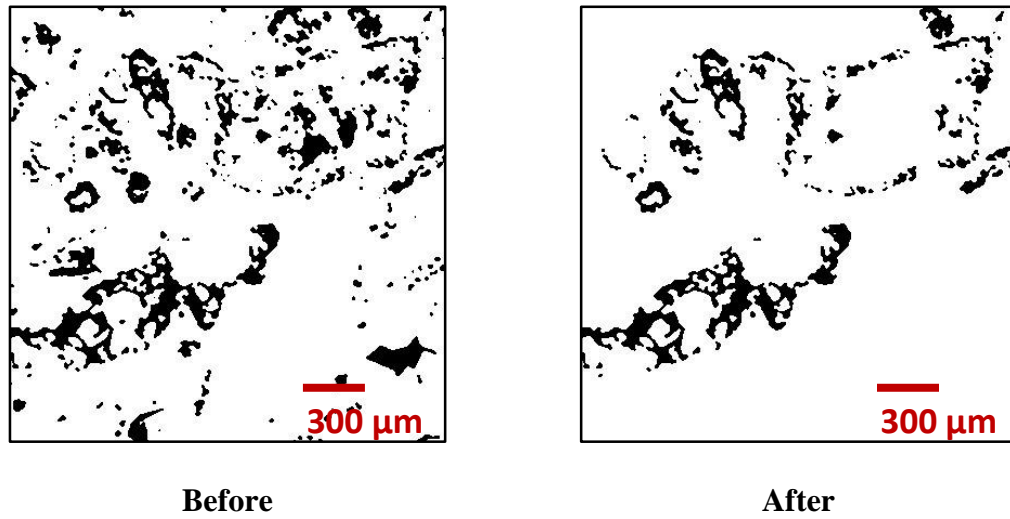
Before   **After**

Figure 3.3— (a) 2D slice of segmented image before and after the purify command was implemented
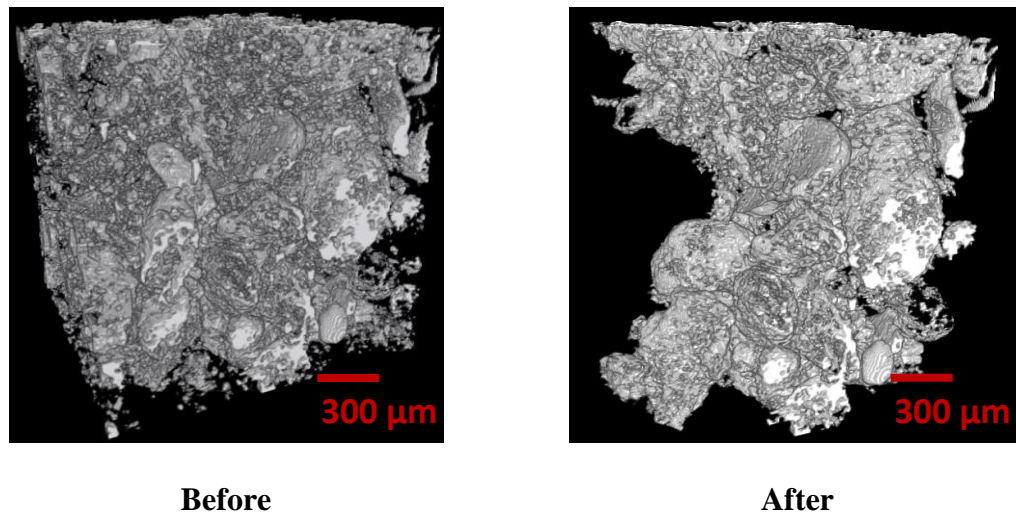
Before   **After**

Figure 3.4— (a) 2D slice of segmented image before and after the purify command was implemented

35

3.5 Results

3.5.1 Electrical Potential Distribution

Figure 3.5 shows an example of the electrical potential distribution within the extracted pore-network of sample 1. The electrical potential at the top and bottom of the pore network were set to boundary conditions of 10 and 0 volts respectively.
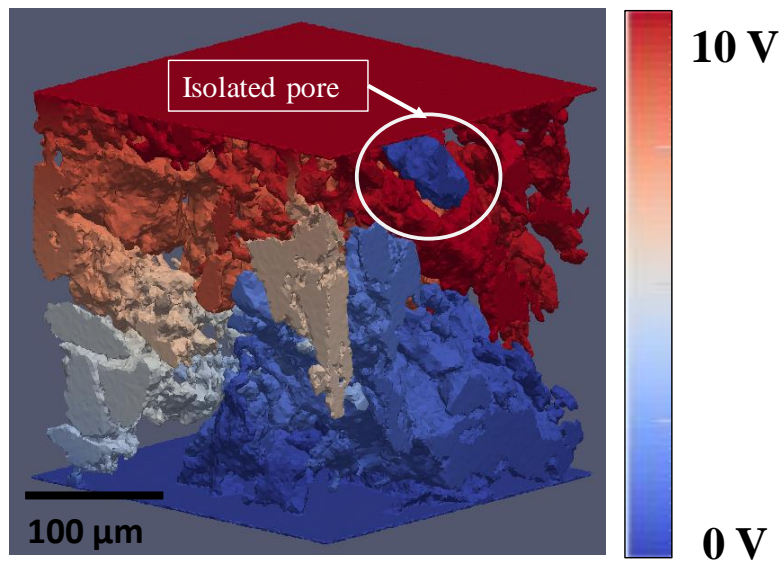
Figure 3.5—Electrical potential distribution in sample 1. The isolated pores are enclosed by non-conductive grains and thus they have zero potential value.

The electrical potential field distribution in the 3D pore-network is very non-uniform as a result of the presence of isolated pores and dead pore-space. The isolated pores in the pore-

network are surrounded by non-conducting grains and therefore assume the zero potential boundary value. Consequently, the potential gradient and electrical current through the isolate pore-space are both equal to zero. In addition to the isolated pores, the pore network also consists of stagnant pore space. Stagnant pore-spaces correspond to portions of the pore space with very low electric potential gradient represented by a marginal change in electric potential. In sample 1, I observed the presence of dead pore-space in the upper right corner of pore network shown in **Figure 3.3**. The electrical potential value in this portion of the pore-space remains relatively constant which indicates very low potential gradient and current flow in this part of the pore-network.

3.5.2 Permeability Assessment

Each micro-CT image was divided into 200^3 voxelized subsamples. The conducting pore-network and permeability of each subsample was numerically derived by simulating fluid and electrical current flow in 3D pore-network. **Figure 3.6(a)** shows the relationship between the directional LBM permeability and the connected porosity for Sample 1 and **Figure 3.6**(b) shows the relationship between the directional LBM permeability and the conducting porosity in xy-direction. **Figure 3.7** (a) and (b) show the same relationships in the z-direction for Sample 1.
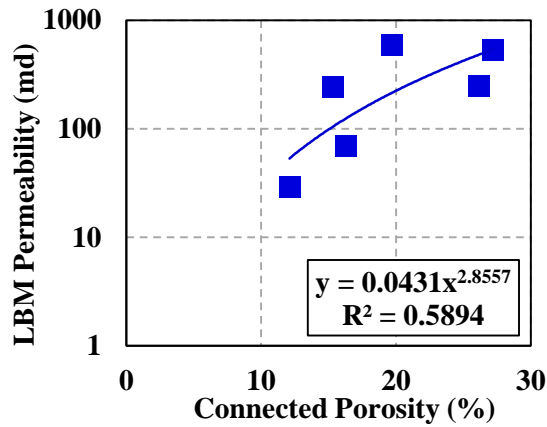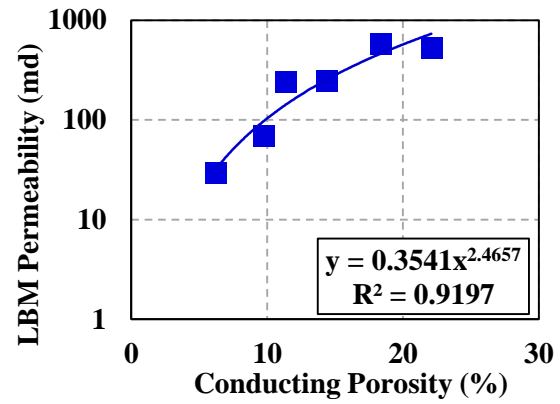
(a)   **(b)**

Figure 3.6—a) Crossplot of the XY-directional LBM permeability and connected porosity in Sample 1 b) Crossplot of the XY-directional LBM permeability and directional conducting pore-network in Sample 1.
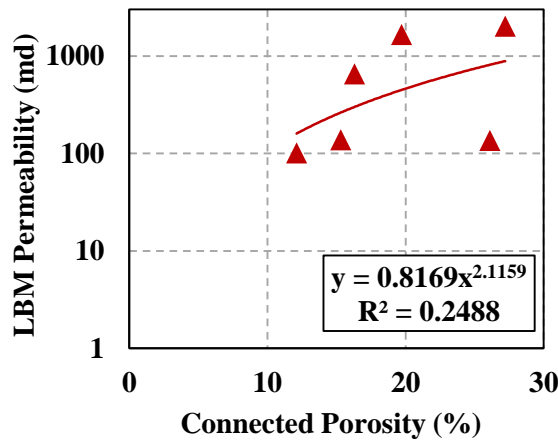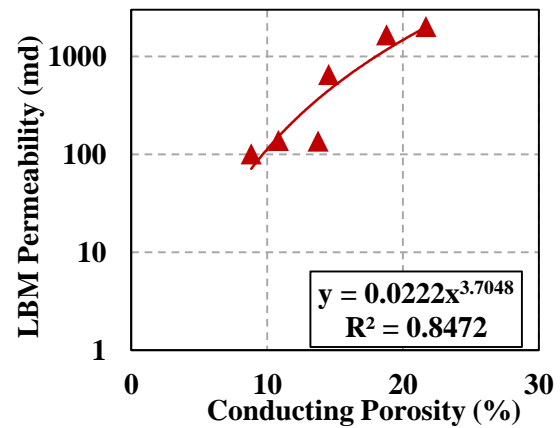
(a)   **(b)**

Figure 3.7—a) Crossplot of the z-direction LBM permeability and connected porosity in Sample 1 b) Crossplot of the z-direction LBM permeability and directional conducting pore-network in Sample 1.

38

The correlations between directional permeability and connected porosity such as the correlations shown in **Figure 3.6**(a) and **Figure 3.7**(a) were used for the assessment of pore-scale directional permeability in each micro-CT subsample. I also estimated the directional permeability using similar correlations between the directional permeability and the directional conducting pore-network (**Figure 3.6**(b) and **Figure 3.7**(b)) for a comparison between the proposed method and conventional permeability assessment techniques. **Figure 3.8(a)** shows the crossplot of the LBM permeability and permeability estimated from the connected porosity while **Figure 3.8(b)** show the crossplot of the LBM permeability and permeability estimated from the directional conducting pore-network. I observed a 54% reduction in the relative error in permeability assessment using the proposed method as compared to conventional permeability assessment techniques.

(a)   (b)
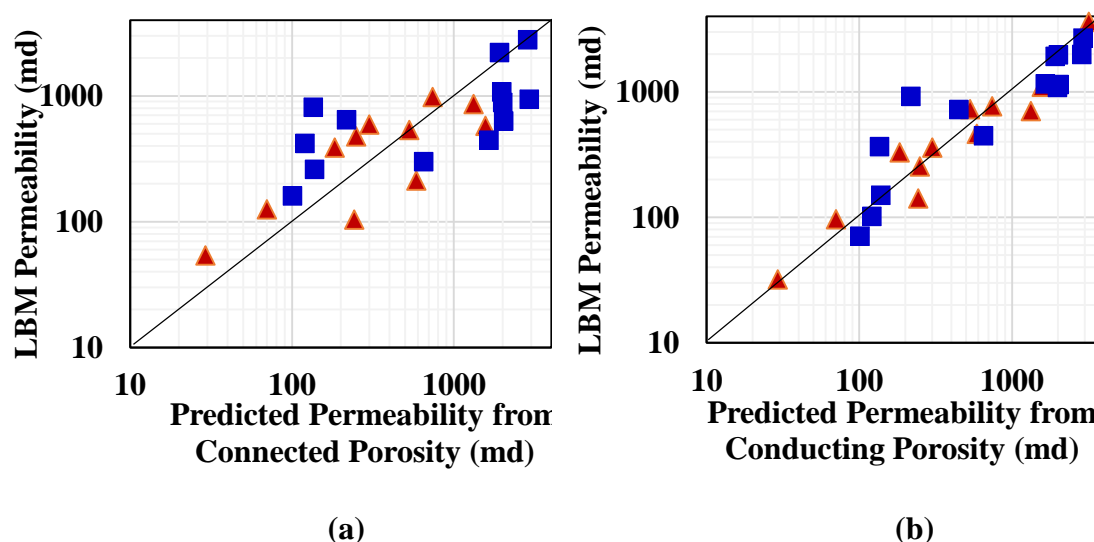
Figure 3.8— (a) Crossplot of the LBM permeability and permeability estimated from the connected porosity (b) Crossplot of the LBM permeability and permeability estimated from the directional conducting pore-network

3.6 Conclusions

A stronger relationship (based on the obtained coefficient of correlation) between directional permeability and directional conducting pore-network, as compared to relationships between permeability and connected porosity. The reason for this result is that fluid flow in carbonate rocks is controlled by directional pore-network connectivity and presence of dead-end spaces, which are more accurately represented by conducting porosity, as compared to connected or total porosity. Although connected porosity is a measure of connectivity in the pore network, it does not account for the presence of poorly connected stagnant pore spaces or the anisotropic rock properties

Consequently, more accurate estimates of directional permeability were obtained using the directional conducting pore-network model as compared to the connected porosity-permeability correlations. I observed a relative improvement of approximately 52% in the pore-scale permeability assessment, compared to the application of connected porosity-permeability correlations.

4. FIELD APPLICATION: SACROC UNIT

Section 3 presented the application of the proposed method for pore-scale assessment of directional permeability in carbonate rocks with complex pore structure. This section presents the application of the proposed method to field example: the SACROC Unit

4.1 Introduction

Carbonate formations consist of a wide range of pore types with different shapes, pore-throat sizes, and varying levels of pore-network connectivity. Such heterogeneous pore-network properties affect the fluid flow in the formation. Characterizing pore-network properties (e.g., effective porosity and permeability) in carbonate formations is, however, challenging due to the heterogeneity at different scales and complex pore structure of carbonate rocks. In this section I use an integrated technique for the multi-scale characterization of carbonate pore structure based on Mercury Injection Capillary Pressure (MICP) measurements, X-ray micro-computed (micro-CT) three-dimensional (3D) rock images, and well logs. The pore types were determined based on the pore-throat radius distributions obtained from MICP measurements. I introduce a new method for assessment of directional conducting pore-network and permeability in the well-log domain, based on pore-scale numerical simulations of fluid and electrical current flows in 3D micro-CT core images, obtained in each pore type. Finally, I use pore-scale derive models for the depth-by-depth conducting pore-network, permeability in the formation.

41

4.2 SACROC Geological Setting

SACROC Unit located in the Midland basin, west Texas. The producing formation in this field is the Canyon Reef, a Pennsylvanian-age limestone. The Canyon Reef has heterogeneous distribution of petrophysical properties, as the result of exposure to high-amplitude sea-level fluctuations (Kane, 1979; Brnak et al., 2006). Geological interpretations show that the SACROC Unit is composed of bedded bioclastic limestone and thin shale beds representing the Strawn, Canyon, and Cisco Groups of the Pennsylvanian

4.3 Micro-CT Image Acquisition and Processing

I obtained high resolution pore-scale images of each pore type use a high resolution micro-CT scanner. I scanned core samples of 2-4 mm in length at a resolution of 2-3μm/voxel. The X-ray source voltage and power is set to 70-80KV, and 5-6 watts, respectively. 5000-6000 projections were acquired over the 360º sample rotations. The resulting images were captured by a flat panel detector and reconstructed using a built-in image processing software package. The final result is a stack of two-dimensional (2D) gray-scale images (**Figure 2**). I converted the gray-scale image stack into a binarized image stack (**Figure 3**). The binarized images were in turn converted into binary digital matrices that serve as input files to the pore-scale numerical simulations.

4.4 Pore-scale Numerical Simulation of Fluid Flow using Lattice Boltzmann Method

I calculated the pore-scale directional permeability by simulating fluid flow in the pore-scale images obtained from each pore type. I used the Lattice Boltzmann method (LBM) to simulate fluid flow in the voxelized micro-CT image. In lieu of solving the macroscopic Navier Stokes equation, the LBM simulates the flow of a Newtonian fluid by discretizing the Boltzmann transport equation on a lattice mesh. I used Palabos (2013), an open-source parallel Lattice Boltzmann solver to simulate single-phase fluid flow in all three directions of the 3D micro-CT image. The permeability in each direction was then calculated from Darcy's law.

4.5 3D Micro-CT Images

Table 1 lists the total voxel image dimensions, resolution, and total porosity of each micro-CT image in each pore type. **Fig. 4.1** shows the 3D micro-CT pore-scale images obtained from each pore type. The pore space in the micro-CT images in pore-type 3 (PT3_S1 and PT3_S2) was not readily visible at a resolution of 2 μm/voxel. Thus, I did not conduct our analysis in pore type 3.

Table 1: 3D Micro-CT Samples with their associated matrix volumes, micro-CT resolutions, total porosity, and pore type. The rock samples are named according to their pore type (PT) and sample number (e.g., PT1_S1 corresponds to the first sample in pore type 1).

Sample Name	Pore	Volume (pixel^3)	Resolution	Total Porosity
PT1_S1	1	1000x1000x2000	2.7	4.00
PT 1_S2	1	600x600x600	2.0	5.80
PT 2_S1	2	600x600x600	2.0	6.00
PT 2_S2	2	600x600x600	2.0	2.87
PT 3_S1	3	900x900x900	2.0	0.60
PT 3_S2	3	900x900x900	2.0	0.20

PT 1_S1   PT 2_S1   PT 3_S1

PT 1_S2   PT 2_S2   PT 3_S2
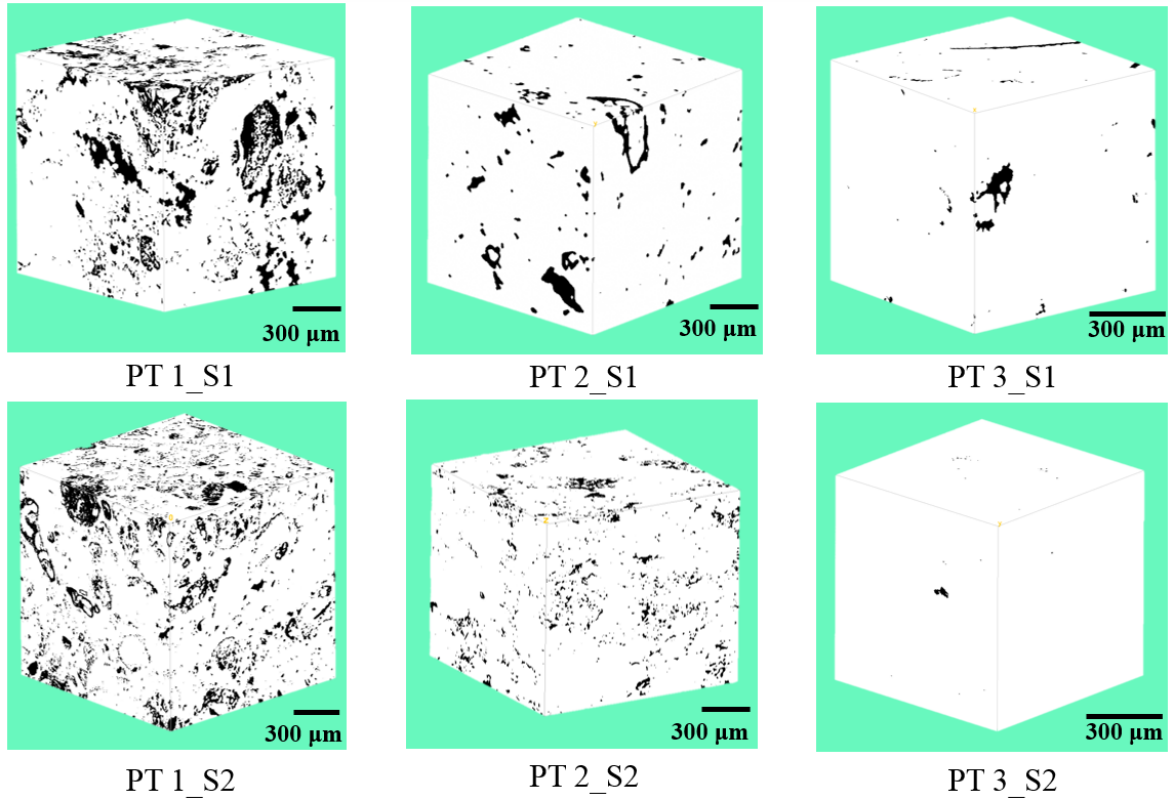
Figure 4.1— The 3D pore-scale images of the six micro-CT samples used in the SACROC Unit. The white and black regions represent the grains and pores, respectively

4.6 Results

Figs. **4.2** and **4.3** show the relationships between permeability and total, connected, and conducting pore-network for pore type 1 and 2, respectively.

(a)

(b)

(c)
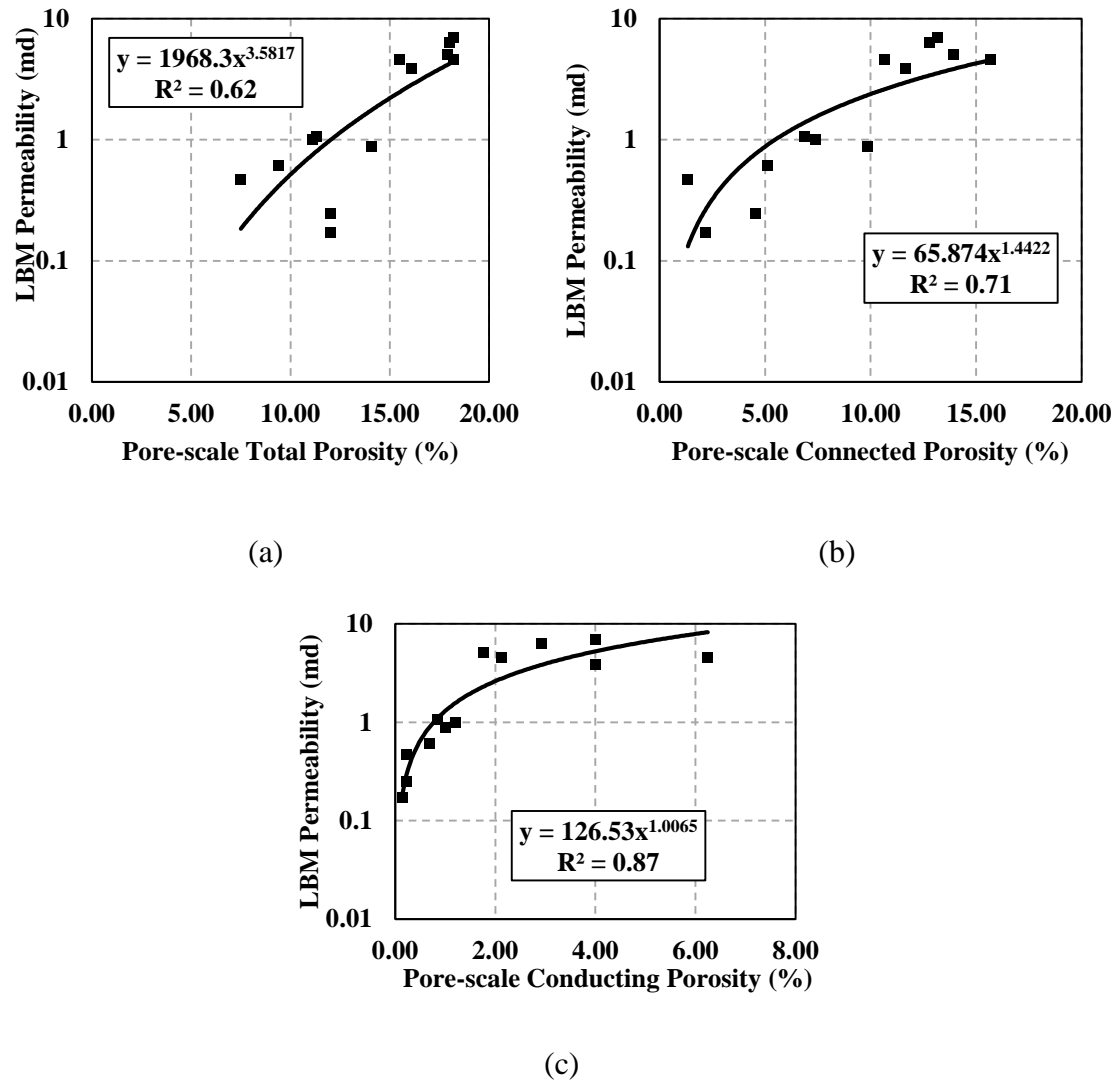
Figure 4.2— Permeability-porosity crossplots for pore type 1: (a) permeability-total porosity crossplot, (b) permeability-connected porosity crossplot, and (c) permeability-effective porosity crossplot.
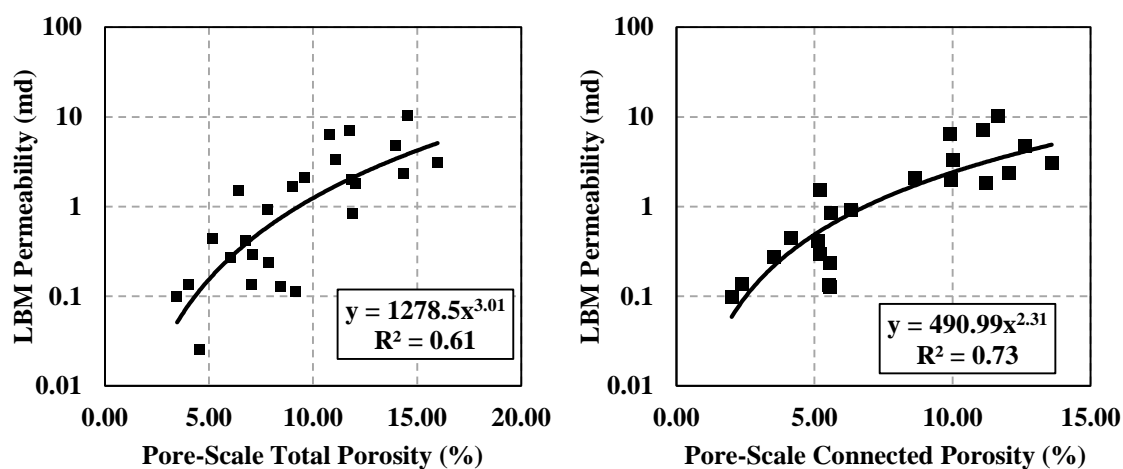
(a)

(b)
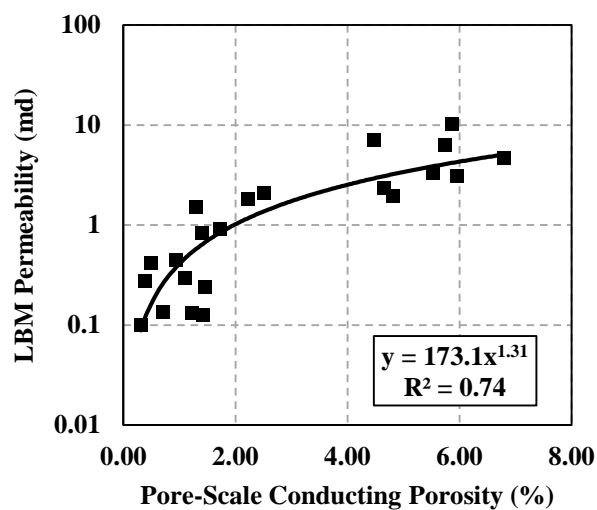
(c)

Figure 4.3— Permeability-porosity crossplots for pore type 2: (a) permeability-total porosity crossplot, (b) permeability-connected porosity crossplot, and (c) permeability-effective porosity crossplot.

Figure 4.4 shows the conducting-resistivity trends for pore types 1 and 2 used for the

assessment of conducting pore-network in the well-log domain.

Pore Type 1

$$y = 14.13x^{-1.013}$$
$$R^2 = 0.9971$$

(a)

Pore Type 2

$$y = 12.336x^{-1.038}$$
$$R^2 = 0.9755$$
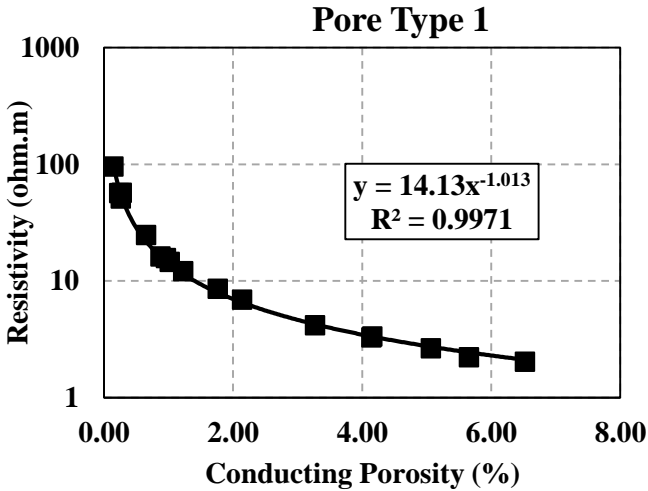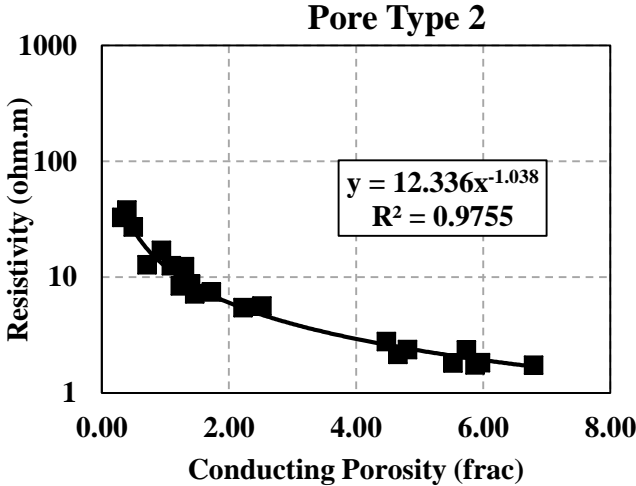
(b)

Figure 4.4— Pore-scale derived relationships between electrical resistivity and conducting pore-network for (a) pore type 1 and (b) pore type 2.

Figure 4.5 shows the final well-log interpretation and permeability assessment results in

the well-log domain.
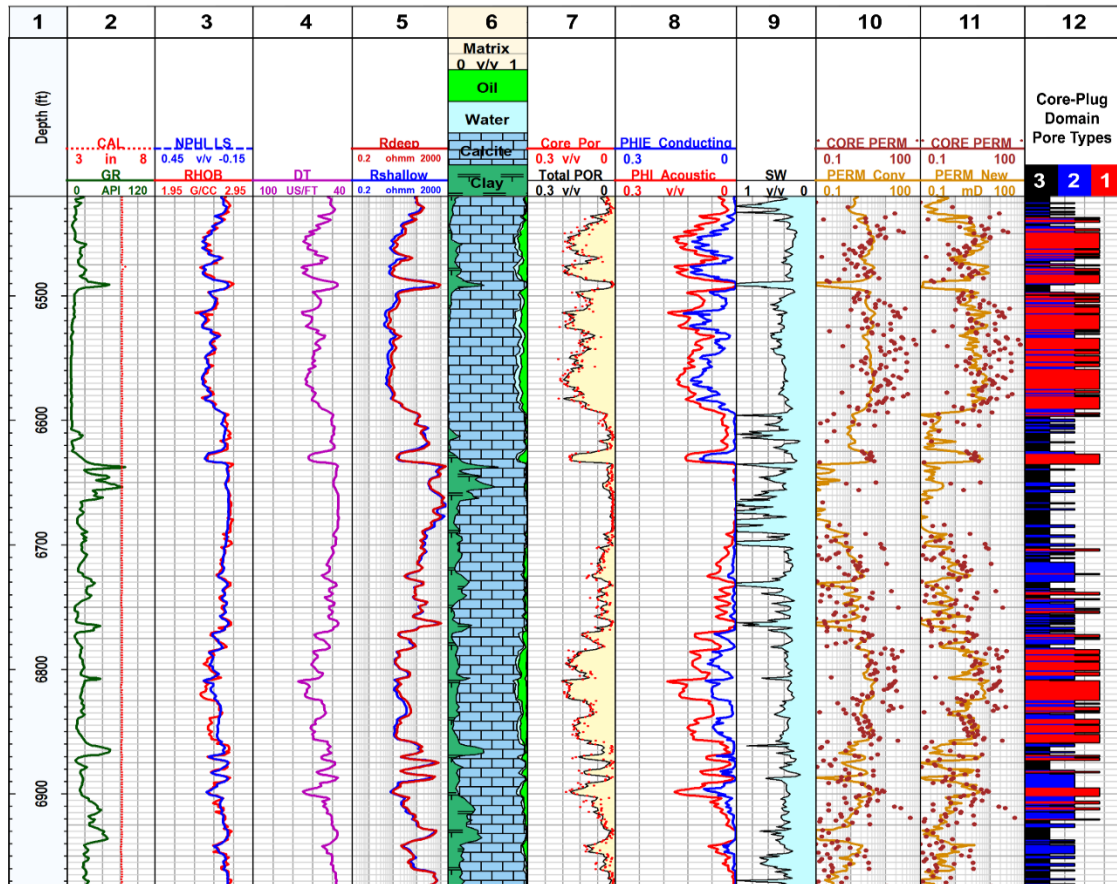
Figure 4.5—SACROC Unit Field Example: conventional well logs and results of well-log interpretation, permeability assessment, and pore typing. Track 1: depth; Tracks 2-5: GR, caliper, neutron porosity (in water-filled limestone units), bulk density, compressional-wave slowness, and apparent resistivity logs; Track 6: estimates of volumetric concentrations of calcite and clay; Track 7: estimates of total porosity, compared to core measurements (red dots); Track 8: estimates of water saturation; Track 9: estimates of connected porosity based on compressional-wave slowness measurements using Wyllie's time-average equation (Wyllie et al., 1956) and estimates of conducting pore-network based on the identified relationships between electrical resistivity and permeability in each pore type; Track 10: estimates of permeability using the core-based porosity-permeability 11: estimates of permeability based on the proposed method; Track 12: identified pore types.(Reprinted from Oyewole et al., 2015)

I calculated the average relative error associated with the permeability estimates obtained

using the proposed method and conventional correlations between core permeability and

total porosity. The average relative error is given by

$$e = \frac{1}{n} \sum_{i=1}^{n} \frac{(k_{est_i} - k_{core_i})}{k_{core_i}}, \tag{25}$$

where k_{core} is the ith core permeability measurement, k_{est} is the ith well-log-based

permeability estimate, n is the total number of core measurements and e is the relative

error in estimates of well-log-based permeability.

I observed a 34% decrease in the relative error associated with the proposed

permeability assessment technique as compared to the application of core-based

correlations between total porosity and permeability (**Figures 4.2 and 4.3**).

4.7 Conclusion

The results demonstrated that electrical resistivity measurements can be applied for direct

assessment of conducting pore-network and permeability, in the presence of numerically

derived pore-scale models and sufficient MICP measurements for initial pore typing. I

observed a relative improvement of approximately 34% in permeability assessment,

compared to the application of core-based correlations between total porosity and

permeability. I also demonstrated that electrical resistivity logs can be used to characterize

the pore-structure in heterogeneous formations. The combination of numerically derived electrical resistivity-conducting pore-network and electrical resistivity-permeability models presented in this research can significantly reduce the need for extensive number of cores for characterization of pore network in carbonate formations. The MICP measurements and pore-scale numerical analysis can be conducted using rock-cuttings, which are smaller in size and readily available as compared to conventional core plugs. Nevertheless, additional core data and incorporation of reliable upscaling techniques can further improve the proposed technique.

5. CONCLUSIONS AND SUMMARY

This thesis introduced a new directional permeability assessment technique in carbonate formations based on conducting pore-network estimated from electrical resistivity measurements. First, I accounted for the heterogeneous distribution of pore types in the formation by performing well-log-based petrophysical rock classification in the formation. Then, I obtained three-dimensional micro-CT images of samples in each rock type. I derived models for the conducting pore-network in each rock type by conducting numerical simulations to measure the electrical conductivity in each micro-CT image. Finally, I applied these models for a depth-by-depth assessment of conducting pore network volume fraction and permeability in the formation.

I successfully applied the proposed technique in various carbonate rocks and in the SACROC (Scurry Area Canyon Reef Operators Committee) Unit. The estimates of permeability in the well-log domain were cross-validated using the available core measurements. I observed a 34% improvement in the relative errors in estimates of permeability (compared to core measurements), as compared to the core-based porosity-permeability models.

I also demonstrated that electrical resistivity logs can be used to characterize the pore structure in heterogeneous formations. The combination of numerically derived electrical resistivity-conducting pore network volume fraction and electrical resistivity-permeability

51

models presented in this thesis can significantly reduce the need for extensive number of cores for characterization of pore network in carbonate formations. The MICP measurements and pore-scale numerical analysis can be conducted using rock cuttings, which are smaller in size and readily available as compared to conventional core plugs. Nevertheless, additional core data and incorporation of reliable upscaling techniques can further improve the proposed technique.

The proposed directional permeability assessment technique can be applied for the well-log-based assessment of directional permeability and conducting pore network volume fraction in carbonate formations with anisotropic petrophysical properties. Furthermore, assessment of directional conducting pore network volume fraction can enhance the interpretation of electrical resistivity logs and the assessment of hydrocarbon saturation in complex carbonate formations. Finally, the introduced method improves reservoir characterization, which has significant influence on completion decisions.

REFERENCES

Ambegaokar, V., Halperin, B. I., and Langer, J. S., 1971, Hopping Conductivity in Disordered Systems: Phys. Rev. B **4**, 2612.

Archie, G.E., 1942, The electrical resistivity log as an aid in determining some reservoir characteristics: Transactions of the AIME, **146**, 54-62.

Bassiouni, Z., and Ogbe, D., 1978, Estimation Of Aquifer Permeabilities From Electric Well Logs: The Log Analyst, **19**, 21-27

Berg, C.F., 2012, Re-examining Archie's law: conductance description by tortuosity and constriction: Physical Review E, **86**, 1-9.

Brie, A., Johnson, D.L., and Nurmi, R.D. 1985. Effect of Spherical Pores on Sonic and Resistivity Measurements: SPWLA 26th Annual Logging Symposium, Dallas, Texas, USA, 17–20 June. Paper W.

Brnak, J., Petrich, B., and Konopczynski, M.R., 2006, Application of smart well technology to the SACROC CO_2 EOR project: Presented at the Symposium on Improved Oil Recovery, SPE.

Carman, P. (1937), Fluid flow through a granular bed: Trans. Inst. Chem. Eng., **15**, 150–167.

Carothers, J. E., 1968, A statistical study of the formation factor relation: Log Analyst, **9**, 5, 13–20.

Chen, S., and Doolen, G.D., 1998, Lattice Boltzmann method for fluid flows: Annual Review of Fluid Mechanics, **30**, 329-364.

Chicheng, X. and Torres-Verdín, C., 2013, Core-based petrophysical rock classification by quantifying pore-system orthogonality with a bimodal Gaussian density function: Presented at the International Symposium, Society of Core Analysts

Choquette, P.W. and Pray, L.C. 1970. Geologic Nomenclature and Classification of Porosity in Sedimentary Carbonates: AAPG, **54**, 207–250.

Clerke, E.A., 2009, Permeability, relative permeability, microscopic displacement efficiency, and pore geometry of m_1 bimodal pore systems in Arab d limestone: SPE Journal, **14**, 3, 524-531.

Clerke, E.A., Mueller III, H.W., Phillips, E.C., Eyvazzadeh, R.Y., and Jones, D.H., 2008, Application of Thomeer hyperbolas to decode the pore systems, facies and reservoir properties of the Upper Jurassic Arab D limestone, Ghawar field, Saudi Arabia: a Rosetta stone approach: GeoArabia , **13**, 4, 113-160.

Coates, G.R. and Dumanoir, J.L., 1974, A new approach to improved log-derived permeability: The Log Analyst, 17-31.

Cover, T.M. and Hart P.E., 1967, Nearest neighbor pattern classification: Transactions of the IEEE, **13**, 1, 21-27.

Dong, H., 2007, Micro-CT imaging and pore network extraction: PhD dissertation, Imperial College London.

Dunham, R.L. 1962. Classification of Carbonate Rocks According To Depositional Texture. American Association of Petroleum Geologists, Memoir 1: 108–121.

Fang, Q., and Boas D.A., 2009, Tetrahedral mesh generation from volumetric binary and gray-scale images: Presented at the Proceedings of ISBI

Fatt, I., Maleki, M., and Upadhyay, R. N., 1966, Detection and estimation of dead-end pore volume in reservoir rock by conventional laboratory tests: SPE Journal, **6**, 3, 206-212.

Garing C., Luquot L., Pezard A.P., and Gouze P., 2014, Electrical and flow properties of highly heterogeneous carbonate rocks: AAPG Bulletin, **98**, 1, 49-66.

Han, W.S., Mcpherson, B.J., Lichtner, P.C., and Wang, F.Pl, 2010, Evaluation of trapping mechanisms in geologic co_2 sequestration: case study of SACROC northern platform, a 35-year CO_2 injection site: American Journal of Science, **310**, 4, 282-324.

Herrick, D.C., and Kennedy, W.D., 2009, A new look at electrical conduction in porous media: A physical description of rock conductivity: Presented at the Annual Logging Symposium, SPWLA.

Huntley, D., Relations between permeability and electrical resistivity in granular aquifers, 1986: Groundwater, **24**, 4,466-474.

Kane, A.V., 1979, Performance review of a large-scale CO_2-WAG enhanced recovery project, SACROC Unit Kelly-Snyder Field: Journal of Petroleum Technology, **31**, 2, 217-231.

Kazatchenko, E., Markov, M., and Mousatov, A. 2003. Determination of Primary and Secondary Porosity in Carbonate Formations Using Acoustic Data: Presented at the SPE Annual Technical Conference and Exhibition, Denver, Colorado, 5-8 October 2003.

Kohonen, T., 2001, The self-organizing map: Springer Series in Information Sciences, **30**, 3, 501-505.

Kosinski, W.K and W.E. Kelly, 1981, Geoelectric soundings for predicting aquifer properties: Ground Water, **19**, 2,163-171.

Kozeny, J., 1927 , Uber kapillare Leitung der Wasser in Boden, Sitzungsber. Akad: Wiss. Wien, **136**, 271–306.

Levenberg, K., 1944, A method for the solution of certain non-linear problems in least squares: Quarterly of Applied Mathematics, **2**, 164-168.

Leverett, M.C. 1941. Capillary Behavior in Porous Solids: Transactions of the AIME, Vol. 142, No. **1**, 159–172.

Lloyd, S.P., 1982, Least squares quantization in PCM: Transactions of the IEEE on Information Theory, **28**, 129-137.

Lonoy, A., 2006, Making sense of carbonate pore systems: AAPG Bulletin, **9**, 1381-1405.

Lucia, F.J., 1995, Rock-fabric/petrophysical classification of carbonate pore space for reservoir characterization: AAPG Bulletin, **79**, 9, 1275-1300.

Lucia, F.J., 2007, Carbonate reservoir characterization. Berlin, Germany, Springer-Verlag.

MacQueen, J.B., 1967, Some methods for classification and analysis of multivariate observations: Proceedings of 5-th Berkeley Symposium on Mathematical Statistics and Probability, Berkeley, University of California Press, **1**, 281-297.

Marquardt, D., 1963, An algorithm for least-squares estimation of nonlinear parameters: SIAM Journal of Applied Mathematics, **11**, 431-441.

Marzouk, I., Takezaki, H., and Miwa, M., 1995, Geologic controls on wettability of carbonate reservoirs: Presented at the Middle East Oil Show, SPE.

Matyka, M. and Koza, Z., 2012, How to Calculate Tortuosity Easily: AIP Conference. Proceedings, **1453**, 17-22

Mazac, O., Kelly W.E., and Landa I., 1985. A hydrogeophysical model for relations between electrical and hydraulic properties of aquifers: Journal of Hydrology, **79**, 16, 123-129.

Øren, P.E. and Bakke, S., 2002, Process-based reconstruction of sandstones and prediction of transport properties: Transport in Porous Media, **46**, 31-343.

Oyewole, E., Saneifar, M., and Heidari, Z., 2015, Multi-Scale Characterization of Pore Structure in Carbonate Formations: Application to the SACROC Unit. Society of Petrophysicists and Well-Log Analysts.

Palabos, 2013, The Palabos software project:

http://www.palabos.org/documentation/tutorial/permeability.html.

Peters, E.J., 2012, Advanced petrophysics, 1 and 2, Austin, Texas: Greenleaf Book Group.

Pittman, E.D., 1992, Relationship of porosity and permeability to various parameters derived from mercury injection- capillary pressure curves for sandstone: AAPG Bulletin, **76**, 2, 191-198.

Purcell, W.R., 1949, Capillary pressures - their measurement using mercury and the calculation of permeability: Transactions of the AIME, 186, 39-48.

Schindelin, J., Arganda-Carreras, I., and Frise, E, Fiji: an open-source platform for biological-image analysis: Nature methods, **9**, 7, 676-682.

Skalinski, M., Gottlib-Zeh, S., and Moss, B., 2005, Defining and predicting rock types in carbonates – preliminary results from an integrated approach using core and log data in Tengiz field: Presented at the 46th Annual Logging Symposium, SPWLA

Skalinski, M. and Kenter, J., 2013, Carbonate Petrophysical Rock Typing: Chevron Patent application, US 2013/0179080 A1.

Skalinski, M. and Kenter, J., 2014, Carbonate petrophysical rock typing: Integrating geological attributes and petrophysical properties while linking with dynamic behavior: The Geological Society of London, **406,** 1, 229-259.

Sok, R.M., Knackstedt, M.A., Varslot T., Ghous, A., Latham, S., and Sheppard, A.P., 2010, Pore scale characterization of carbonates at multiple scales: Integration of Micro-CT, BSEM, and FIBSEM: Petrophysics, **51**, 6, 379-387.

Theologou, P.N., Skalinski, M., and Mallan, R.K., 2015, An MICP-based pore typing workflow – core scale to log scale: Presented at the 56th Annual Logging Symposium, Long Beach, SPWLA.

Thomeer, J.H.M., 1960, Introduction of a pore geometrical factor defined by the capillary pressure curve: Journal of Petroleum Technology, **12**, 3, 73-77.

Thompson, A., Katz, A.J., and Krohn, C.E., 1987, The microgeometry and transport properties of sedimentary rock: Advances in Physics, **36**, 625-694.

Timur, A., 1968, An investigation of permeability, porosity and residual saturation relationship for sandstone reservoirs: The Log Analyst, **9**, 4, 8.

Tixier, M.P, 1949, Evaluation of permeability from electric-log resistivity gradients: Oil & Gas Journal, pp. 113.

Vik, B., Djurhuus, K., Spildo, K., and Skauge, A., 2007, Characterization of Vuggy Carbonates. SPE/EAGE Reservoir Characterization and Simulation Conference, Abu Dhabi, UAE, October 28–31. SPE-111434.

Walsh, J. B., and W. F. Brace, 1984, The effect of pressure on porosity and the transport properties of rock: Journal of Geophysics, **89**, B11, 9425–9431

Wempe, W. A., and Mavko, G. 2002, Effective porosity - total porosity model applied to Fontainebleau sandstone: SEG Annual Meeting, Salt Lake City, Utah, USA, 6–11 October.

Winsauer W. O., Shearin H.M., Masson P.H., Resistivity of brine-saturated sands in relation to pore geometry: Bull. Am. Assoc. Petrol. Geologists, 36, p. 278, 1952

Wyllie, M. R. J., and Rose, W.D., 1950, Some theoretical considerations related to the quantitative evaluation of the physical characteristics of reservoir rock from electrical log data : Trans. Am. Inst, Mech. Eng., 189, 105-118.

Wyllie, M. R. J., and Spangler, M. B., 1952, Application of Electrical Resistivity Measurements to Problem of Fluid in Porous Media: ibid., Vol. **36**, p. 359.

Wyllie, M.R.J., Gregory A.R., and Gardner, L.W., 1956, Elastic wave velocities in heterogeneous and porous media: Geophysics, **21**, 41-70.